



# Pushover Analyses of Slender Cantilever Bridge Piers with Strength and Ductility Degradation

Paolo Di Re<sup>a</sup>, Davide Bernardini<sup>b</sup>, Daniela Ruta<sup>b</sup>, and Achille Paolone<sup>a</sup>

<sup>a</sup>Dept. of Structural and Geotechnical Engineering, Sapienza University of Rome, Rome 00184, RM, Italy

<sup>b</sup>Dept. of Structural and Geotechnical Engineering, Sapienza University of Rome, Rome 00197, RM, Italy

## ARTICLE HISTORY

Received 9 May 2023  
Revised 30 August 2023  
Accepted 1 October 2023  
Published Online 6 January 2024

## KEYWORDS

Bridge piers  
Reinforced concrete  
Pushover  
Moment-curvature response  
Corrosion  
Geometric nonlinearity

## ABSTRACT

Reinforced concrete bridge piers are often subject to spatially non-uniform deterioration which typically produces strength and ductility degradation. When piers are subject to deterioration, the sectional response is no longer uniform and the determination of the pushover curves from sectional response is no longer immediate. This paper proposes a simplified procedure to accomplish this task for RC bridge cantilever piers. The method is simplified only with respect to geometric nonlinearities and yields an accurate estimate of the ultimate displacement, free of numerical issues typical of fiber-based finite elements. The procedure is based on an iterative approach to enforce the element equilibrium under P-Delta effects induced by vertical loads and can consider arbitrary deterioration patterns through the specification of different moment-curvature response along the elevation. After validating the approach with experimental results, a parametric analysis of the influence of sectional strength and ductility degradation is carried out for the case study of a rectangular hollow RC pier. Results show that significant variations of the pier equivalent plastic hinge length can be expected because of the occurrence of deterioration in the lower part of the pier. Moreover, paper provides quantitative measure of the extent of the strength and ductility degradation.

## 1. Introduction

Reinforced concrete (RC) bridge piers are often subject to strength and ductility degradation due to rebar corrosion (Meda et al., 2014; Rinaldi et al., 2022; Lignola et al., 2023). This has a significant influence on the seismic performances and, thus, computation of capacity curves for deteriorated piers is crucial for the assessment of existing bridges (Domaneschi et al., 2020; Mahboubi and Kioumars, 2021). This requires detailed nonlinear modeling to describe the structural response up to collapse, especially when the ultimate displacement is of interest (Kashani et al., 2019; Castaldo et al., 2022). Fiber-based finite element analysis is a common and useful approach for this task. However, when accurate ultimate displacement is needed, this approach may fail due to issues related to damage localization and mesh sensitivity. Moreover, RC piers often present an additional complexity, as deterioration can develop in a significantly non-uniform way, depending on environmental conditions (Li et al., 2018).

For cantilever piers, representing a special but very common

case (Chen et al., 2020), it is possible to compute pushover curves from the sectional response. However, when piers are subject to non-uniform deterioration, the sectional response is non-uniform along the pier, even for uniform cross-section geometry and reinforcement. Moreover, for slender piers, nonlinear geometric effect may become relevant (Burgueno et al., 2016).

Modeling of reinforced concrete piers subject to corrosion has been studied in detail (Kashani et al., 2019). In Bernardini et al. (2021), a multi-level modeling procedure tailored to describe arbitrary corrosion patterns by means of fiber beam-column elements has been proposed. In Bernardini et al. (2022), the approach has been implemented in a web-based application. In Bernardini et al. (2023), a first set of parametric analyses has been carried out. These studies show that corrosion can produce significant reduction of sectional strength and ductility, so that piers subject to spatially non-uniform corrosion patterns can be analyzed as structures with non-uniform sectional responses.

In these situations, the evaluation of pier ultimate displacement is extremely difficult by fiber-based analysis. In a previous paper

(Di Re et al., 2022), a simple numerical procedure to compute force-displacement curves of cantilever piers taking into account geometric nonlinearities is proposed and validated by comparing the results with both numerical and experimental reference solutions. The procedure is based on the curve parameterization with respect to the curvature of the base cross-section, which is assumed as independent variable driving the analysis. This gives a significant computational advantage under geometric nonlinearities. In fact, while for linear geometry the horizontal force can be clearly used as driving variable, when P-Delta effects are considered, the peak of the horizontal force is reached when the base moment is lower than the sectional strength. Thus, in the post-peak part of the global response, the force is expected to decrease, while bending moments keep increasing (Gaiotti and Smith, 1989; Fenwick et al., 1992; Barros et al., 2010; Babazadeh et al., 2016).

In this work, the procedure is extended to piers with variable piece-wise uniform sectional response, i.e., by dividing the pier into uniform portions with different cross-section bending response. This extension is useful to describe, not only piers where cross-section geometry or reinforcement changes along the height, but also piers subject to spatially non-uniform corrosion.

Pushover curves of corroded piers, of course, can be directly computed also by means of fiber-based finite element analysis of the structure which, however, can be affected by numerical localization phenomena. These may have a significant influence on the evaluation of the ultimate displacements of the structure. The proposed simple procedure can therefore also be used as a control tool for more detailed analyses.

After a short presentation of the numerical procedure, an experimental validation test is described. Then, a parametric analysis of the influence of sectional strength and ductility degradation is performed.

## 2. Numerical Procedure for the Pushover Analysis of Piers with Piece-Wise Uniform Sectional Response

A straight cantilever pier subject to self-weight  $q$ , and vertical  $P$  and horizontal  $F$  forces at the top is considered (Fig. 1(a)). This is modeled as Euler-Bernoulli beam, hence assuming that its aspect ratio is sufficiently high to neglect transverse shear deformations. The inclusion of the shear deformations, although possible, requires a significant modification of the governing equations and will be addressed in future works.

The pier is partitioned into  $m$  pieces (Fig. 1(b)), each characterized by uniform bending moment-curvature response, previously determined from a separate computation:

$$M = f_j(K) \quad \text{with } j \in [B, 1, 2, \dots, m-1]. \quad (1)$$

Sectional responses are assumed to monotonically increase so that all functions in Eq. (1) are invertible and the peak moment  $M_{j,p}$  and the corresponding curvature  $K_{j,p}$  are uniquely determined (Fig. 2). Hence, the procedure describes the pier behavior until cross-sections reach their peak bending moment, which is often

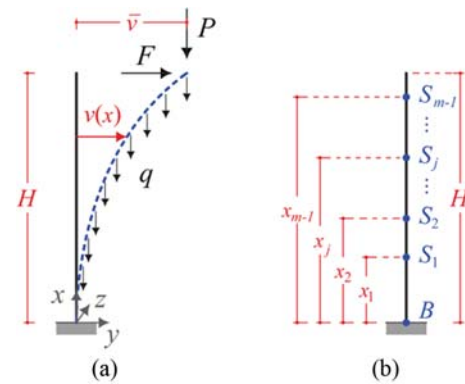


Fig. 1. Schematic Representation of the Pier Model: (a) Reference and Deformed Configurations, (b) Partition Defining the Piece-Wise Uniform Sectional Response of the Pier

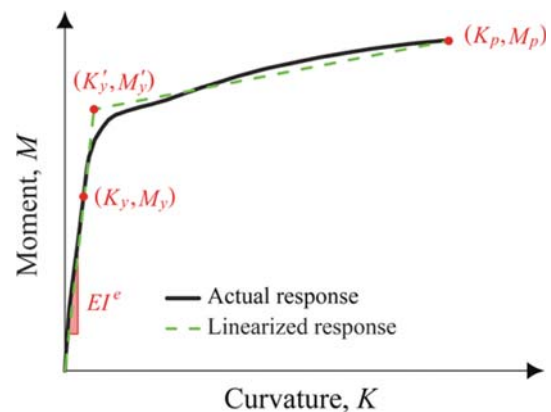


Fig. 2. Typical  $M$ - $K$  Response of RC Bridge Pier Cross-Sections

sufficient to reach collapse. The inclusion of an eventual softening part of the  $M$ - $K$  response is possible but requires additional considerations and assumptions that are beyond the scope of this paper.

To be noted is that the definition of functions  $f_j$  can be accomplished in several ways, depending on the information available on the pier and the user knowledge. In this work, numerical simulations based on fiber cross-section models are used. However, also analytical approaches can be considered. For fast preliminary computations, bilinear or trilinear  $M$ - $K$  relationships can be defined by manually computing the significant points of the cross-section response.

Given a bending moment profile  $M(x)$ , the corresponding curvature profile  $K(x)$  can be computed by the combined evaluation of the inverses of all Eqs. (1):

$$K(x) = f_{j_x}^{-1}[M(x)] \quad \text{with } j_x \in [B, 1, 2, \dots, m-1], \quad (2)$$

where  $j_x$  denotes the piece to which the cross-section  $x$  belongs and  $f^{-1}$  is the inverse of the sectional response.

The algorithm for the computation of the pier pushover curve, described in Table 1, is an extension of that reported in Di Re et al. (2022) and the reader can refer to this paper for further details. The procedure is based on the iterative enforcement of equilibrium with various estimates of transverse displacement profile, neglecting

**Table 1.** Detail of the Algorithm for the Numerical Computation of the Pushover Curve of the Pier. Superscripts  $n$  and  $i$  Indicate Quantities Computed at Current Pushover and Iteration Step, Respectively

1)	while $K_B^n \leq K_{B,p}$ increment $K_B^n = K_B^{n-1} + \Delta K_B^n$
2)	$M_B^n = f_B[K_B^n]$
3)	Iteration initialization: $v_0^n(x) := v^{n-1}(x)$
4)	$F_i^n = \frac{M_B^n - P\bar{v}_{i-1}^n - q \int_0^H v_{i-1}^n(x) dx}{H}$
5)	$M_i^n(x) = F_i^n(H-x) + P[\bar{v}_{i-1}^n - v_{i-1}^n(x)] + q \int_x^{H-x} [v_{i-1}^n(\xi) - v_{i-1}^n(x)] x \xi$
6)	$K_i^n(x) = f_{j_x}^{-1}[M_i^n(x)] \text{ with } j_x \in [B, 1, 2, \dots, m-1]$
7)	$\theta_i^n(x) = \int_0^x K_i^n(\xi) d\xi$
8)	$v_i^n(x) = \int_0^x \theta_i^n(\xi) d\xi$
9)	$\bar{v}_i^n := v_i^n(H)$
10)	$r_i^n := \frac{\int_0^H \Delta v_i^n(x) dx}{\int_0^H \Delta v_{i-1}^n(x) dx} + \frac{\int_0^H \Delta M_i^n(x) \Delta K_i^n(x) dx}{\int_0^H \Delta M_{i-1}^n(x) \Delta K_{i-1}^n(x) dx} \quad \text{with} \quad \Delta \blacksquare_i := [\blacksquare_i^n(x) - \blacksquare_{i-1}^n(x)]$
11)	If $r > \textit{tolerance} \rightarrow i = i + 1 \rightarrow 4)$ else $\rightarrow v^n(x) := v_i^n(x) \rightarrow n = n + 1 \rightarrow 1)$

the influence of vertical displacements and deformations on the equilibrium. The curvature of the base cross-section  $K_B$  is the control parameter incremented in a step-by-step fashion, from zero to the value  $K_{B,p}$  corresponding to the peak moment  $M_{B,p}$ . At the generic pushover step  $n$ , given  $K_B^n$ , the bending moment at the base is computed via Eq. (1) and iteration begins after the initialization  $v_0^n(x) := v^{n-1}(x)$ . At the  $i$ -th iteration, the transverse displacement profile estimated at previous iteration  $v_{i-1}^n(x)$  is used to compute the horizontal force that ensures global equilibrium, according to:

$$F_i^n = \frac{M_B^n - P\bar{v}_{i-1}^n - q \int_0^H v_{i-1}^n(x) dx}{H} \quad (3)$$

This force can then be used to compute the corresponding bending moment profile:

$$M_i^n(x) = F_i^n(H-x) + P[\bar{v}_{i-1}^n - v_{i-1}^n(x)] + q \int_x^{H-x} [v_{i-1}^n(\xi) - v_{i-1}^n(x)] d\xi, \quad (4)$$

which, in turn, can be used to estimate the curvature profile by means of Eq. (2).  $\xi$  is used as dummy abscissa in place of  $x$  for the integration change of variable. Finally, double integration of the obtained  $K_i^n(x)$  yields a new estimate of the transverse displacement profile  $v_i^n(x)$ , being  $\theta_i^n(x)$  the cross-section rotation profile. Displacements  $v_i^n(x)$  are then used to check convergence. For this purpose, various types of residual can be used; among them, a mixed indicator  $r$  based on a combination of the norms of displacement profile and internal work is proposed, as indicated in Table 1. The value of  $r = 10^{-7}$  is used for all the analyses of this work. Once convergence is reached at pushover step  $n$ , the displacement profile  $v^n(x)$  determines the top displacement

$\bar{v}^n := v^n(H)$  and the corresponding moment  $M^n(x)$  and curvature  $K^n(x)$  profiles. Thus, the next pushover step starts.

The procedure is implemented in a Python script where Simpson quadrature rule is used to solve all integrals along the pier axis.

Notably, the influence of the superstructure could also be included by adopting standard approaches, such as those discussed in Bimschas (2010). In this case, a rotational spring is included at the top of the pier to account for the flexural and/or torsional rigidity of the superstructure, with proper modification of Eqs. (3) and (4).

### 3. Curvature Profiles and Plastic Hinge Length

The proposed procedure produces as output the pier force-displacement curve ( $F-\bar{v}$ ) but also the moment and curvature profiles, from which local axial strains in concrete and steel can be computed, thanks to cross-section planarity, and used to evaluate the proximity to collapse.

Moreover, another information that can be obtained as a by-product of the proposed procedure is the equivalent plastic hinge length  $L_c$ , useful in the definition of detailed nonlinear numerical models (Scott and Fenves, 2006; Di Re and Addessi, 2022; Pozo et al., 2022). The length  $L_c$  can be computed from the curvature profile by the classic approach by Park and co-authors (Park and Paulay, 1975; Priestley et al., 2007; Bae and Bayrak, 2008; Billah and Alam, 2016; Pokhrel and Bandelt, 2019).

During the pushover analysis, after a cross-section reaches its yielding curvature, a region of length  $L_{pr}$  above that cross-section starts to experience inelastic deformations (Fig. 3). Further load increases cause progressive enlargement of this region, which

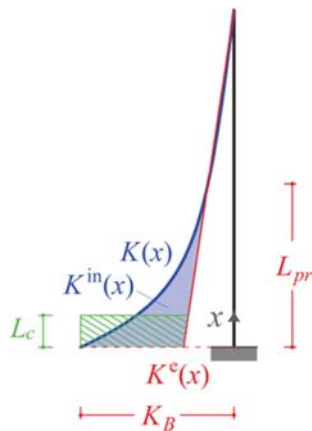


**Fig. 3.** Reference Scheme for the Determination of the Equivalent Plastic Hinge Length

continues until the more stressed cross-section reaches the peak bending moment. At this stage, plastic region has its maximum extension, as bending moments cannot further increase, and force  $F$  must eventually drop.

A typical curvature profile is shown in Fig. 3 (blue curve) where the red line represents the elastic contribution. This can be computed by means of the initial stiffness as:  $K^e(x) = M(x)/EI^e$ . The inelastic curvature (shaded area in Fig. 3) is then given by:

$$K^{is}(x) = K(x) - K^e(x), \quad (5)$$

and the plastic region is the set of cross-sections where  $|K(x)| > |K^e(x)|$ . The equivalent length  $L_c$  is defined as the length of the zone where a uniform curvature equal to  $K_B$  would produce a rotation  $\theta_c = K_B L_c$  equal to the one produced by the inelastic curvature. Accordingly:

$$L_c = \frac{\theta^{in}}{K_B} = \frac{\int_0^{L_{pr}} \left[ K(x) - \frac{M(x)}{EI^e} \right] dx}{K_B}. \quad (6)$$

#### 4. Experimental Validation of the Proposed Model

The proposed procedure can be used to model piers with variable concrete cross-section geometry or reinforcements. In this work, a different application is proposed to study the response of piers where the variability of the sectional response is due to non-uniform corrosion.

This Section validates the accuracy of the proposed approach by comparing numerical solutions with experimental results. The case study of a square RC column is considered (Fig. 4(a)) from the experimental campaign in Rinaldi et al. (2022). The column has a total height from the footing extrados equal to  $H + H_t = 1.8$  m, section width  $b = 30$  cm and it is reinforced with  $4\phi 16$  longitudinal bars and  $\phi 8/250$  transverse stirrups. Both plain and deteriorated specimens are studied (labeled as A25 and B25 in Rinaldi et al. (2022)). For the latter, artificial corrosion is applied to a portion of the column of  $L_0 = 60$  cm from the footing, until 20% of the steel mass loss is averagely reached.

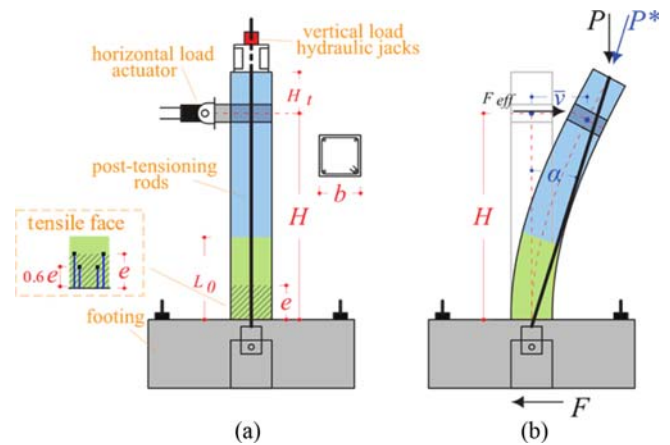


**Fig. 4.** Experimentally Tested RC Column from Rinaldi et al. (2022): (a) Specimen Geometry, (b) Loading Scheme

The specimen is subject to a constant vertical force  $P^* = 300$  kN, applied through external post-tensioning rods that follow the lateral deformation of the column, and a cyclic horizontal force  $F_{eff}$  acting, under displacement control, at  $H = 1.5$  m from the footing (Fig. 4(b)). During the test, the applied horizontal force and the transverse displacement of the loaded point  $\bar{v}$  are recorded. Moreover, the maximum bending moment and curvature at the column base are computed. The latter is obtained from the measured deformations of four potentiometric transducers and is given as mean value of the curvature over a length  $e = 25$  cm. The transducers located on the face under tension are indicated by the blue bars in Fig. 4(a) and are applied at 15 cm (the two internal ones) and 25 cm (the two external ones) from the footing.

Figure 5 shows the envelopes of the positive parts of the cyclic  $M$ - $K$  responses (solid curves). These are plotted with the results of the analytical model in Rinaldi et al. (2022) and obtained by either neglecting (dotted curves) or including (dashed curves) the steel bond slip.

These analytical results are used as input data for the application of the proposed procedure, where the  $M$ - $K$  curves are truncated to the peak bending moment. A single piece associated with the

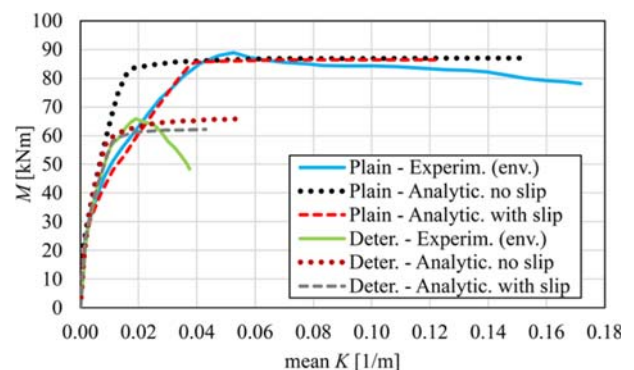


**Fig. 5.**  $M$ - $K$  Response Curves Considered for the Numerical Analysis of the Experimentally Tested RC Column

plain  $M$ - $K$  response is considered for the analysis of the plain specimen, while for the deteriorated case, the pier is divided into two pieces, associated with the deteriorated response ( $L_0$ ) and the plain response ( $H - L_0$ ), respectively. The inclusion of the bond slip in the proposed procedure is accomplished by adopting the analytical  $M$ - $K$  response for the base cross-section where the effects are accounted for.

As the input curves are given in terms of mean curvature over the length  $e$ , for this test, the procedure is slightly modified to comply with these experimental data. The modifications are applied as follows: referring to Table 1, at each iteration, Eq. (2) is used at Step 6 to evaluate the curvature profile; before processing Step 7, this profile is modified by enforcing that all cross-sections in length  $e$  exhibit the same curvature value, equal to that assumed at the base ( $K_B^n$ ). This coincides to assume that the base curvature  $K_B$ , used as input quantity, doesn't correspond to the value of the base cross-section but to the mean value of the base portion  $e$ , as measured in the experimental tests.

Furthermore, due to the method used to apply the axial load, the direction of the constant force  $P^*$  changes when pier deforms (Fig. 4(b) and Babazadeh et al. (2016)). Therefore, the vertical component  $P = P^* \cos \alpha$  varies during the loading process and the applied force  $F_{eff}$  differs from the horizontal resisting force  $F$  of the column, that is:

$$F_{eff} = F + P^* \sin \alpha. \tag{7}$$

Therefore, the procedure is applied following the scheme

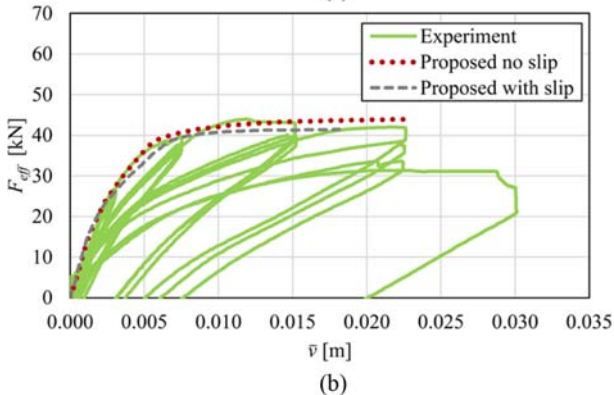
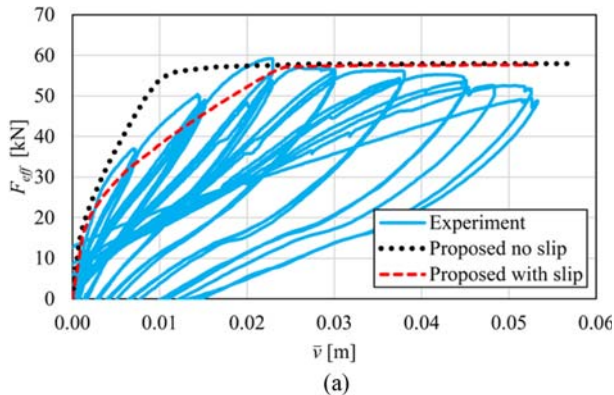


Fig. 6. Numerical Response of the Experimentally Tested RC Column: (a) Plain Material, (b) Deteriorated Material

described in detail in Di Re et al. (2022).

Figure 6 compares the numerical and experimental responses in terms of applied load  $F_{eff}$  versus transverse displacement  $\bar{v}$ . These agree very well, confirming the accuracy of the proposed procedure. The initial stiffness, maximum load bearing capacity and ultimate displacement of the column are well captured, although the final softening part of the response is not reproduced due to the specific assumption of monotonically increasing  $M$ - $K$  response.

The comparison also shows that steel bond slip significantly influences only the pre-peak behavior of the column and, for this test, has limited effects in the deteriorated specimen. However, a complete description of this phenomenon requires further analyses that are beyond the scope of this work.

### 5. Two-Parameters Description of the Deterioration Effects

For RC piers, deterioration produces reduction of strength and ductility at the sectional level (Rinaldi et al., 2008), as also confirmed by the experimental test considered in the previous Section (Fig. 6(a)). For sake of completeness, Fig. 7 shows the envelope of all  $M$ - $K$  response curve obtained in Rinaldi et al. (2022), where two plain and two deteriorated specimens are studied.

In real structures, deterioration may occur in a different way in the various pieces of the pier. However, for cantilever piers, deterioration patterns involving the base portion of the pier are the most severe. A detailed description of this issue is given in Priestley et al. (2007) and further details of a currently ongoing research study on this topic are reported in Bernardini et al. (2021, 2023).

The goal of the following analyses is to numerically investigate the consequences of sectional strength and ductility degradation on the global structural response of the pier and provide useful information that can be used to check and control the results of more refined analyses.

To perform a simple parametric analysis,  $M$ - $K$  curves are assumed to be bilinear, thinking them as suitable bilinearizations of actual nonlinear responses (Fig. 2). In general, the bilinear moment-curvature diagrams of a Plain (P) and a Deteriorated (D)

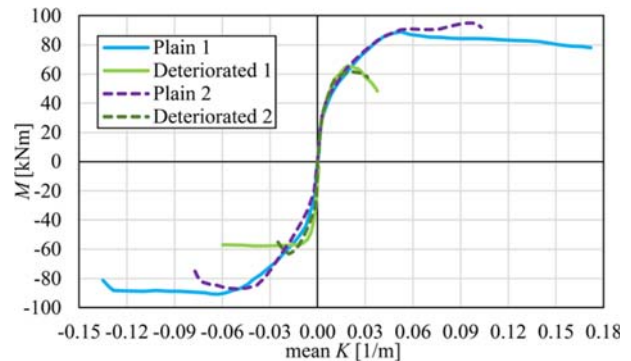
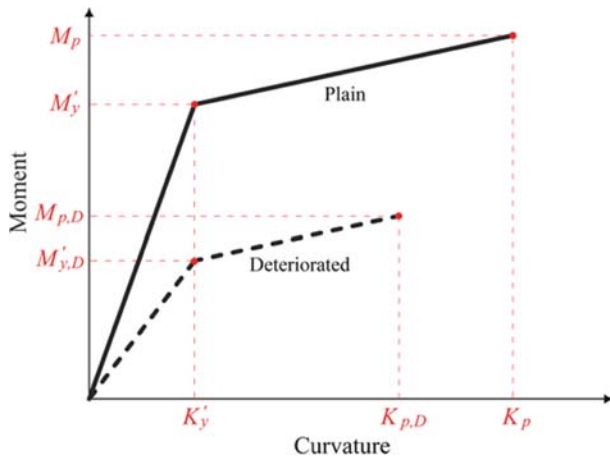


Fig. 7.  $M$ - $K$  Response Curves Obtained for the Two Experimental Tests Reported in Rinaldi et al. (2022)



**Fig. 8.** Effects of Deterioration on the Sectional  $M$ - $K$  Response

cross-section are characterized by 8 parameters:  $(K'_y, M'_y, K_p, M_p)$  and  $(K'_{y,D}, M'_{y,D}, K_{p,D}, M_{p,D})$ . A simple description of the sectional effects of deterioration can be obtained after the introduction of two simplifying assumptions, according to Priestley et al. (2007), derived from experimental observation of common deteriorated pier behavior. First, yielding curvature of plain and deteriorated sections are assumed to be the same. Second, the post-yield slope in the  $M$ - $K$  plane is likewise considered the same in both cases (Fig. 8). Accordingly, the following constraints on the 8 governing parameters hold:

$$K'_{y,D} = K'_y, \quad (8)$$

$$M'_{y,D} = \alpha M'_y, \quad (9)$$

$$K_{p,D} = \beta K_p, \quad (10)$$

$$M_{p,D} = \alpha M'_y + \frac{M_p - M'_y}{K_p - K'_y} (\beta K_p - K'_y), \quad (11)$$

where  $\alpha \in [0; 1]$  and  $\beta \in [0; 1]$  are nondimensional parameters determining, respectively, yielding moment and peak curvature degradation. Therefore, the case of  $\alpha = 1$  and  $\beta = 1$  corresponds to the plain cross-section, whereas cross-sections with various levels of strength or ductility degradation are described by different values of the two parameters.

## 6. The Case Study of an Hollow Rectangular RC Pier

A cantilever RC pier 15 m tall with hollow rectangular cross-section is considered (Fig. 9). The geometry is that of typical piers built in the 1970s in Italy, extracted from a database of more than a thousand piers currently under investigation. The pier has sectional and global aspect ratios equal to  $L_y/L_z = 1.8$ ,  $H/L_y = 3.33$ ,  $H/L_z = 6$  and a longitudinal reinforcement ratio equal to 0.488%, close to that typically observable in existing constructions of this age.

The moment-curvature response of the plain pier (Fig. 10) along both the  $z$ -axis (strong direction) and the  $y$ -axis (weak

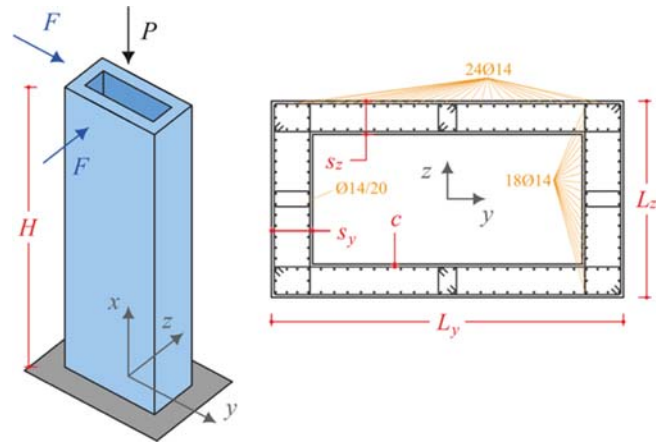


**Fig. 9.** Details of Pier Cross-Section: External size  $L_y = 4.5$  m and  $L_z = 2.5$  m; Thicknesses  $s_y = 50$  cm and  $s_z = 40$  cm; Concrete Cover  $c = 3$  cm; Longitudinal Bars Diameter 14 mm; Stirrup Diameter 12 mm; Stirrup Spacing 200 mm

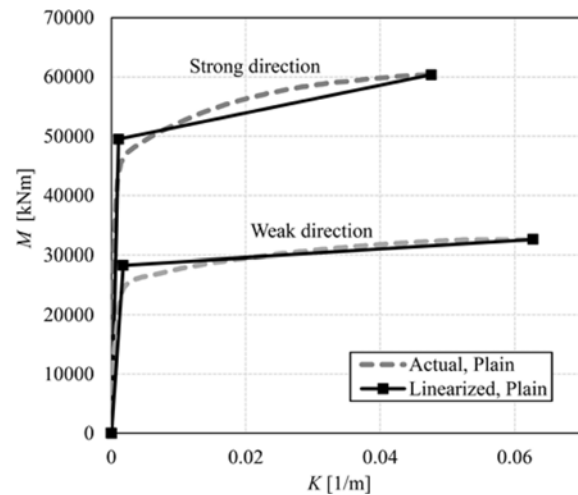


**Fig. 10.** Moment-Curvature Responses Used for the Plain Pier

direction), under axial load  $P$  corresponding to  $P/A_c f_c = 0.0496$ , is computed by means of a fiber discretization developed in OpenSees (2021). The fiber model is based on Kent-Scott-Park ('Concrete02') uniaxial material for concrete and 'ReinforcingSteel' for longitudinal bars (Di Re et al., 2022) with concrete strength and steel yield stress equal to 38 MPa and 508 MPa, respectively. Confinement is taken into account by Mander model (Mander et al., 1988), consistently with the given stirrup layout in Fig. 9. The response of the pier is computed first for the case of plain cross-sections and then under different deterioration scenarios as described in Section 8.

Moment-curvature diagrams in Fig. 10 are used to perform the pushover analysis in the two directions, considering the whole pier as a single piece under the action of load  $P$ . Results are first compared with those of a force-based beam-column finite element model with fiber cross-section discretization, defined in OpenSees, to check whether the variation of cross-sectional response induced by axial-bending interaction would be relevant.

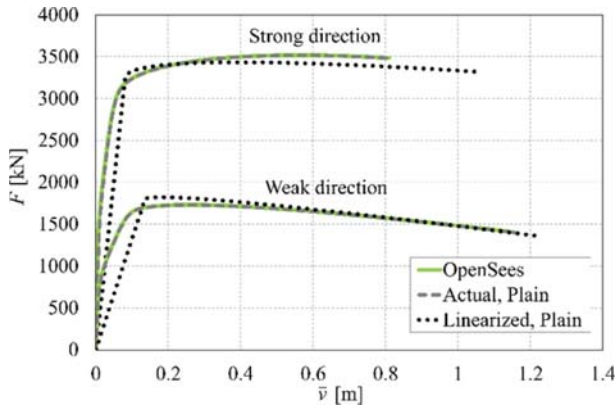


Fig. 11. Pushover Response Curves Obtained for the Plain Pier

The comparison shows excellent agreement (OpenSees vs Actual, Plain in Fig. 11) hence confirming the plausibility of the hypothesis to neglect the influence of axial strains adopted in the proposed procedure.

Geometric nonlinearities are more relevant for weak loading direction than strong one (Fig. 11). Indeed, the softening response shown in the curves is all due to the geometrically nonlinear behavior.

To be noted is that, to obtain an accurate estimate of the element capacity for the strong loading direction, the interaction of the shear strength with the flexural behavior of the pier should be also considered, due to the low aspect ratio  $H/L_y = 3.33$ . Several approaches have been proposed in the literature for this purpose, e.g., Ceresa et al. (2007); Bairan and Mari (2007); Saritas and Filippou (2009); Delgado et al. (2009); Cassese et al. (2017); Di Re et al. (2018); Cassese et al. (2019). Among them, that suggested by Cassese et al. (2019) is very effective as it simply computes the actual capacity of the pier as the point-by-point minimum curve between the flexural and the shear resistance curve of the member. However, this issue is beyond the scope of this paper and the analyses are limited to the evaluation of flexural capacity of the element.

### 7. Influence of the Bilinearization of the Sectional Response

To apply the setting in Section 5, the pushover analysis of the plain pier is repeated after replacement of the actual  $M-K$  diagrams with their bilinearizations (Fig. 10) to carry out a critical analysis of the influence of the bilinearization. The obtained global responses are reported in Fig. 11 as black dotted curves and Table 2 summarizes the main parameters for the two cases.

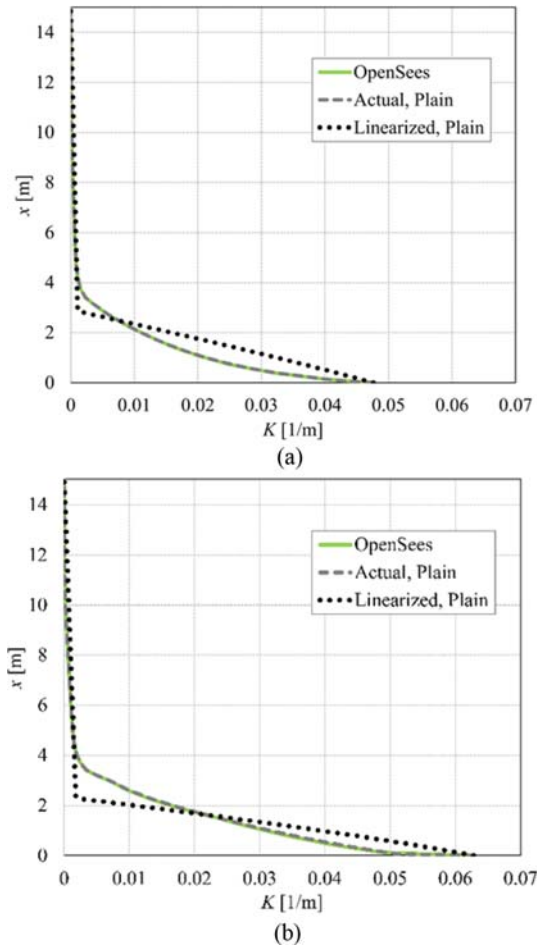


Fig. 12. Variation of Bending Curvature,  $K(x)$ , at End of the  $F - \bar{v}$  Response for the Plain Rectangular Hollow Pier: (a) Strong  $y$ -Direction, (b) Weak  $z$ -Direction

The comparison shows that, whereas the approximation in terms of strength is very good, that of ultimate displacement is worst. This can be understood by checking the curvature profiles in Figs. 12(a) and 12(b) and considering that small differences in the curvature profiles can produce significant differences on the top displacements.

Moreover, with the linearized  $M-K$  response, the length of the inelastic region  $L_{pr}$  tends to be underestimated since the bilinearization produces a yielding moment  $M'_y$  greater than its actual value  $M_y$  (Fig. 10). Accordingly, the size of the inelastic portion of the pier is reduced. However, from Figs. 12(a) and 12(b), it turns out that the differences between the curvature profiles can have opposite sign which partially compensate each other in the computation of the equivalent plastic hinge length  $L_c$ ,

Table 2. Peak Force,  $F_p$ , Ultimate Displacement,  $\bar{v}_u$ , Inelastic Region Length,  $L_{pr}$  and Equivalent Plastic Hinge Length,  $L_c$ , Computed for the Plain Pier

Loading direction	Actual $M-K$				Linearized $M-K$			
	$F_p$ [kN]	$\bar{v}_u$ [m]	$L_{pr}$ [m]	$L_c$ [m]	$F_p$ [kN]	$\bar{v}_u$ [m]	$L_{pr}$ [m]	$L_c$ [m]
Strong, $y$	3515	0.82	4.44	1.13	3432	1.06	2.82	1.48
Weak, $z$	1729	1.16	4.50	1.20	1822	1.21	2.28	1.22

especially in the weak direction.

### 8. Parametric Analysis and Deterioration Scenarios

A parametric analysis of the influence of the deterioration is carried out by using the two-parameter description introduced in Section 5. Although the approximations associated with the bilinearization of the  $M-K$  response may be significant for a single analysis, especially in terms of ultimate displacement, the comparison between the pier response under different deterioration scenarios, all with linearized sectional response, is expected to be a good approximation of the actual relative response.

The deterioration scenarios considered in the parametric analysis are based on a spatially non-uniform pattern, with deterioration taking place from the base of the pier up to an elevation  $L_0 = 3\text{ m}$  (Fig. 13), a value chosen to be slightly bigger than the value  $L_{pr}$  of the undamaged pier. The procedure is then applied by considering the pier partitioned into two pieces. The piece bounded by the base cross-section is associated with a bilinear  $M-K$  response characterized by values of  $\alpha$  and  $\beta$  representing deterioration states (Section 5). The second piece is associated with the bilinearized plain  $M-K$  diagram.

In this setting, the parametric analysis is carried out by letting the parameters  $\alpha$  and  $\beta$  to vary from 1 (plain) to 0.25 (severe degradation), through six discrete values (1, 0.85, 0.7, 0.55, 0.4, 0.25). Overall, 36 different combinations of strength and ductility degradation are explored, as depicted in the scheme of Fig. 14, where a few particular conditions are highlighted by colored dots. Specifically, red dots correspond to the case of pure sectional Strength Degradation (SD) with  $\beta = 1$  and variable  $\alpha$ , blue dots correspond to the cases of pure sectional Ductility Degradation (DD) with  $\alpha = 1$  and variable  $\beta$ , and orange dots correspond to Mixed Degradation (MD) where both SD and DD occur in the same proportion. Finally, upper and lower diagonal grey dots describe cases in which there is mixed degradation

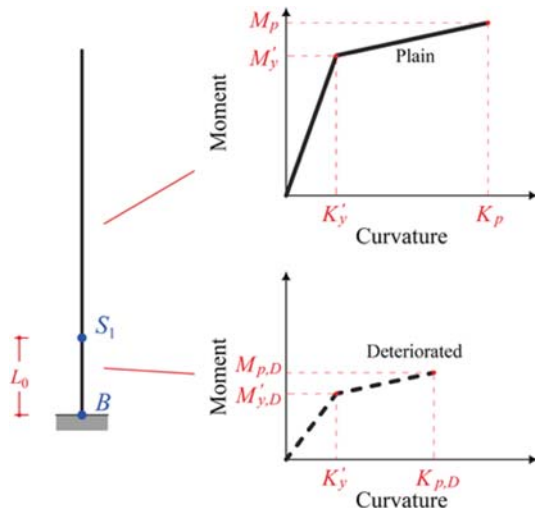


Fig. 13. Computational Schemes Adopted for the Rectangular Hollow Pier and Schematic of  $M-K$  Response Modification

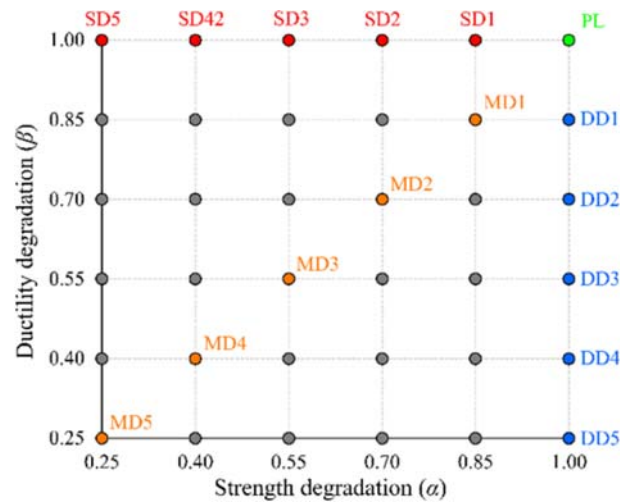


Fig. 14. Schematic Representation of the Deterioration Scenarios Considered in the Parametric Analysis

with prevalence of one of the two sources.

### 9. Influence of Sectional Deterioration on Pier Response

The results of the parametric analysis are discussed first in terms of global strength and ductility and then in terms of curvature profiles and plastic hinge length.

#### 9.1 Residual Strength and Ductility

Global  $F - \bar{v}$  response curves obtained by pushing along the strong direction are shown in Fig. 15 for (a) the SD and (b) DD scenarios.

The pure sectional strength degradation (SD) scenarios ( $\alpha < 1$  with  $\beta = 1$ ) are characterized by a reduction of pier strength essentially proportional to  $\alpha$  and to an increase in ductility (Fig. 15(a)). The latter is due to the fact that, under the hypotheses depicted in Section 5, when the yielding moment is reduced, the constancy of yielding curvature induces a reduction of sectional stiffness which, in turn, produces a small reduction of pier stiffness and a significant increase in the ultimate displacement.

In the more severe scenarios (SD3-5), characterized by values of  $\alpha = 0.55, 0.4, 0.25$ , the pier becomes more flexible so that softening effects due to geometric nonlinearity become relevant. The ultimate displacement occurs at force levels significantly lower than peak force. In such conditions, technical codes, e.g., European Committee for Standardization (2005), suggest defining, conventionally, ultimate displacement as the value corresponding to a shear force reduction of 15% with respect to its peak value. Therefore, a conceptual distinction is introduced between the actual and utilizable displacement capacity of the pier. The former corresponds to the attainment of the ultimate limit state, which here is assumed to occur when the base cross-section reaches its peak curvature. The utilizable displacement capacity is reached when the shear force drops to  $0.85F_p$ , being  $F_p$  the



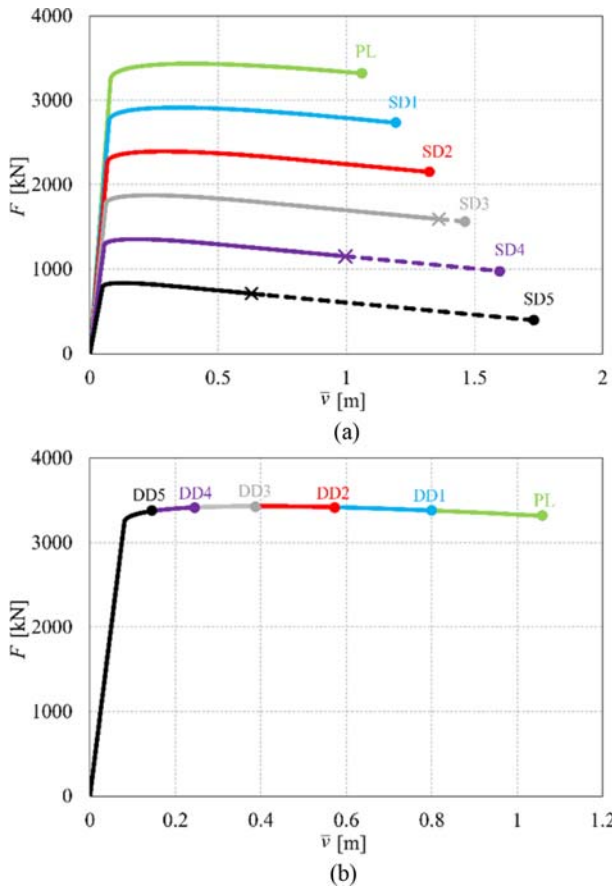


**Fig. 15.** Pier Response in the Strong  $y$ -Direction for the: (a) Pure SD, (b) Pure DD Scenarios (dots and crosses respectively indicate the achievement of actual and utilizable ultimate displacement)

peak value. Clearly, this distinction becomes significant only when softening effects are relevant because, otherwise, actual capacity is fully utilizable. To describe this aspect, in Fig. 15(a) and subsequent ones, the points corresponding to the utilizable displacement capacity are marked by a cross and the part of the curves leading to the actual capacity are indicated by a dashed line.

The pure sectional ductility degradation (DD) scenarios ( $\alpha = 1$  with  $\beta < 1$ ) does not produce reduction of the pier strength as the various curves follow the same post-elastic path (Fig. 15(b)). However, a non-proportional reduction of ultimate displacement is observed. For example, the scenario DD4, characterized by a sectional ductility reduction of 75%, produces a reduction of the pier ductility of about 86%.

Mixed degradation (MD) scenarios, shown in Fig. 16 for both loading directions, produce a reduction of both pier strength and ductility. Fig. 16(b) shows the results in the weak direction where, due to the lower stiffness of the pier, softening effects are more evident leading to a clear distinction between actual and utilizable ductility.

To better appreciate the results, it is useful to consider pier strength and utilizable ductility observed under a given deterioration scenario, normalized with respect to the corresponding values for

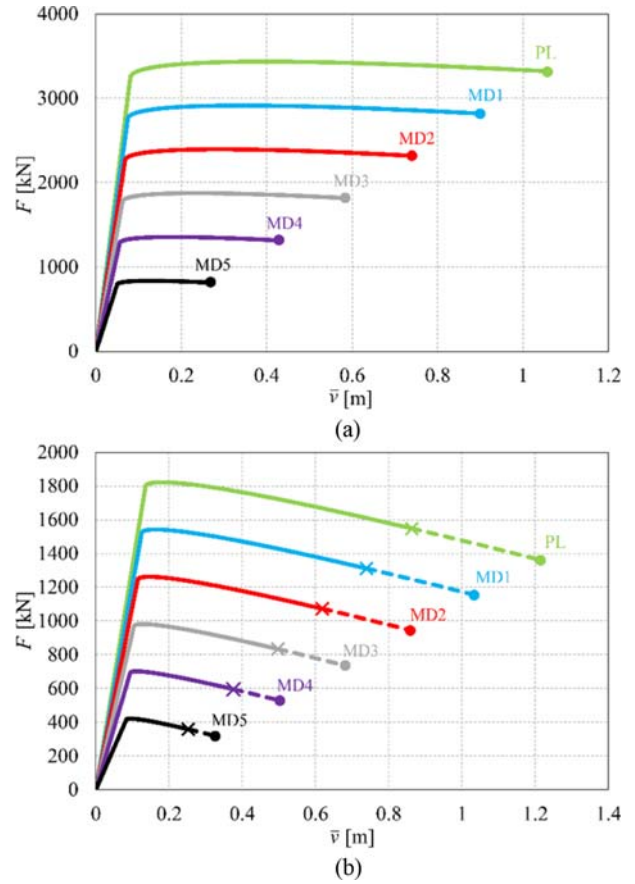


**Fig. 16.** Pier Response for the MD Scenarios: (a) Strong  $y$ -Direction, (b) Weak  $z$ -Direction

the plain pier, as expressed by the two nondimensional parameters: Residual Pier Strength (RPS):

$$RPS = \frac{S_d}{S_{PL}} \tag{12}$$

Residual Pier Ductility (RPD):

$$RPD = \frac{\mu_d}{\mu_{PL}} \tag{13}$$

Analysis of the tables in Figs. 17(a) and 17(c) confirms the above remark. On the other hand, from Figs. 17(b) and 17(d) it is evident that residual utilizable pier ductility is strongly dependent on both  $\alpha$  and  $\beta$  in a nonlinear way and that, in some conditions, global deterioration may be stronger than the sectional one. For example, RPD turns out to be lower than sectional ductility degradation  $\beta$  for lower values of sectional strength reduction. For example, for  $\beta = 0.25$ , RPD can be as low as 0.14 or 0.16 for bigger values of  $\alpha$ . In contrast, for  $\alpha < 1$  but  $\beta = 1$ , the mentioned increase of the ultimate displacement produces an increase of the pier ductility, which can reach almost 130% of the plain value (in Figs. 17(b),  $RPD > 1$ , for  $\alpha < 1$  and  $\beta = 1$ ).

The variation of RPD with respect to both parameters  $\alpha$  and  $\beta$  is fully described by the plots in Fig. 18. This figure, together with the tables in Figs. 17, are useful to have a summary idea of

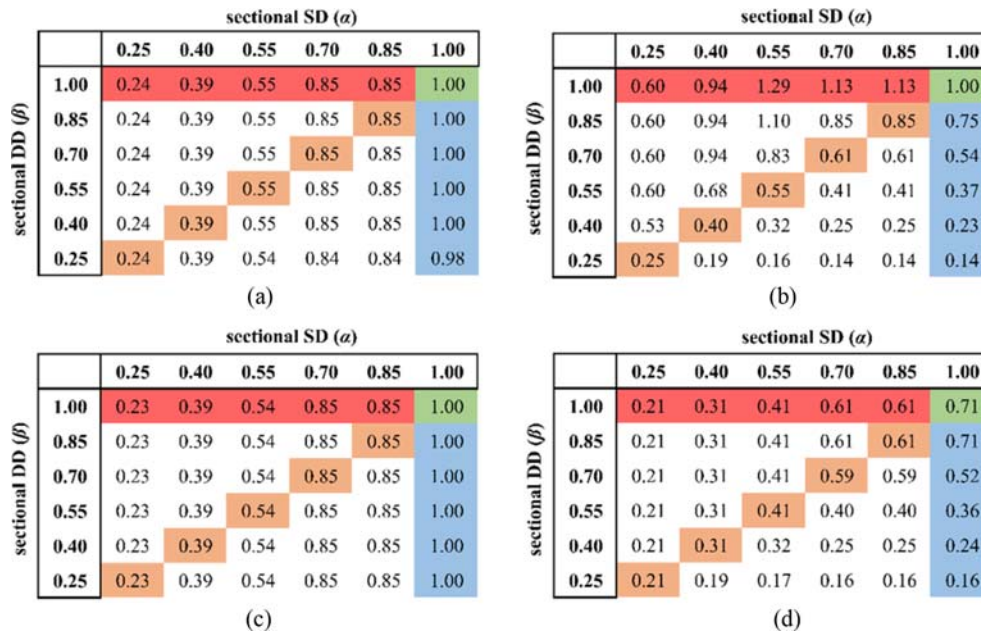


Fig. 17. Summary of Residual Pier Capacity for the Considered Scenarios in Both Loading Directions: (a) RPS for Strong y-Direction, (b) RPD for Strong y-Direction, (c) RPS for Weak z-Direction, (d) RPD for Weak z-Direction

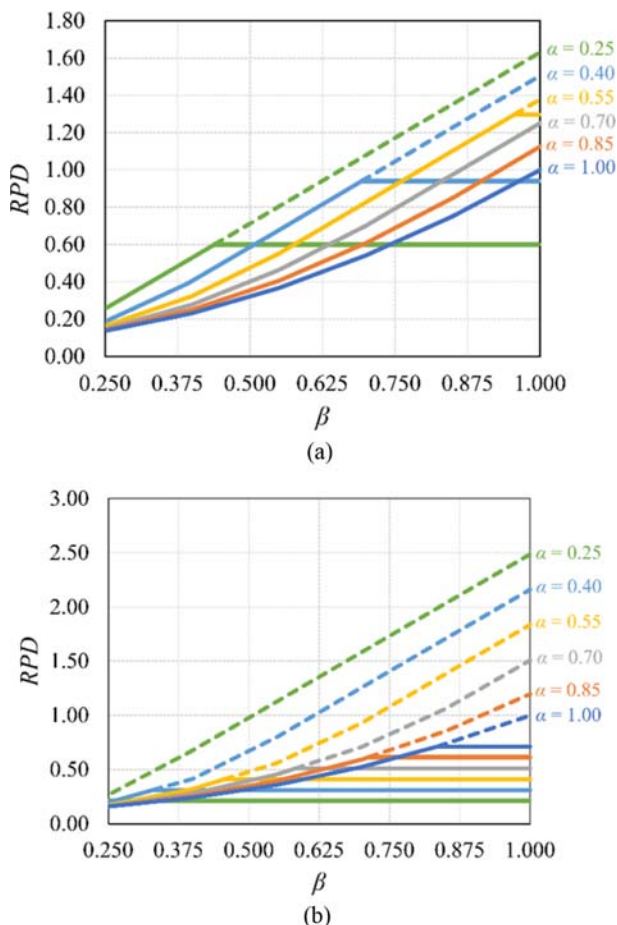


Fig. 18. Residual Pier Ductility as a Function of Sectional Ductility Degradation for Various Values of  $\alpha$  (dashed curves represent conditions where utilizable ductility is less than the actual one): (a) Strong y-Direction, (b) Weak z-Direction

the extent of strength and ductility degradation in relation with the cross-section performance loss, i.e., of the material degradation.

## 9.2 Curvature Profile and Plastic Hinge Length

Figure 19 shows the curvature profiles evaluated at the final stage of the loading process in the strong direction. Subfigure (a) compares the profile of the plain pier with the ones of the scenarios SD1 and SD2. Although the  $M-K$  response does not encounter softening and localization phenomena, the spread of inelastic bending curvature tends to localize in the lower deteriorated part of the pier, with the upper part remaining elastic (Figs. 19(a) and 19(b)). A jump in the curvature occurs at the beginning of the deteriorated zone with intensity increasing with  $\alpha$ , as shown in Fig. 19(b). Since ultimate curvature remains constant while SD scenarios produce jumps in the curvature at the beginning of the deteriorated zone, the length of the inelastic region  $L_{pr}$  remains constant but length  $L_c$  increases due to the wider area underneath the profile in the inelastic zone. However, even if  $L_c$  increases it never exceeds the height  $L_0$  of the deteriorated part.

Figure 20 shows the ultimate curvature profiles for the DD scenarios in the strong direction. In such conditions, the inelastic curvature profiles of the deteriorated piers are shifted with respect to the plain ones, with consequent reduction of both  $L_{pr}$  and  $L_c$ .

Figures 21 and 22 summarize the variations of the plastic hinge length  $L_c$  normalized with respect to the pier height. Dashed curves represent the variation of  $L_c$  computed by referring to the actual ultimate displacement, for the cases where this is reached after the utilizable one (solid curves). Results show that significant variations in the plastic hinge length can be expected because of sectional degradation, especially for loading in the strong

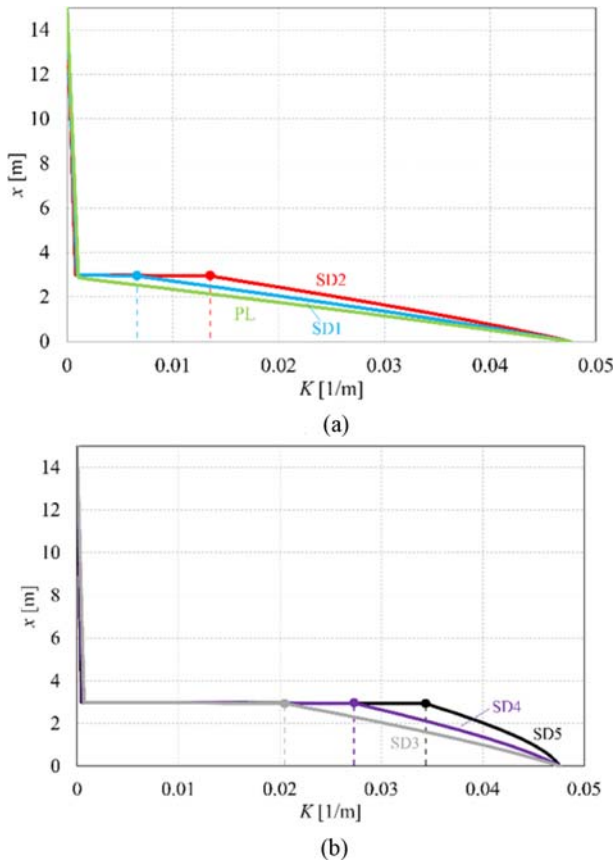


Fig. 19. Curvature Profiles for the SD Scenarios (strong y-direction): (a) PL, SD1 and SD2, (b) SD3, SD4 and SD5

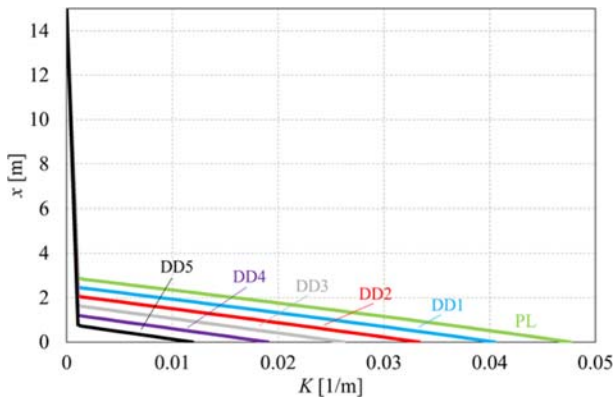


Fig. 20. Curvature Profiles for the DD Scenarios (strong y-direction)

direction.

### 10. Conclusions

A simple numerical procedure for the computation of the force-displacement response of cantilever piers with arbitrary sectional behavior distribution was proposed. This is particularly useful for piers characterized by non-uniform corrosion. In these conditions, the evaluation of strength deterioration can be estimated by fiber-based analysis, however that of ultimate displacement may be not accurate due to localization issues. By contrast, the proposed

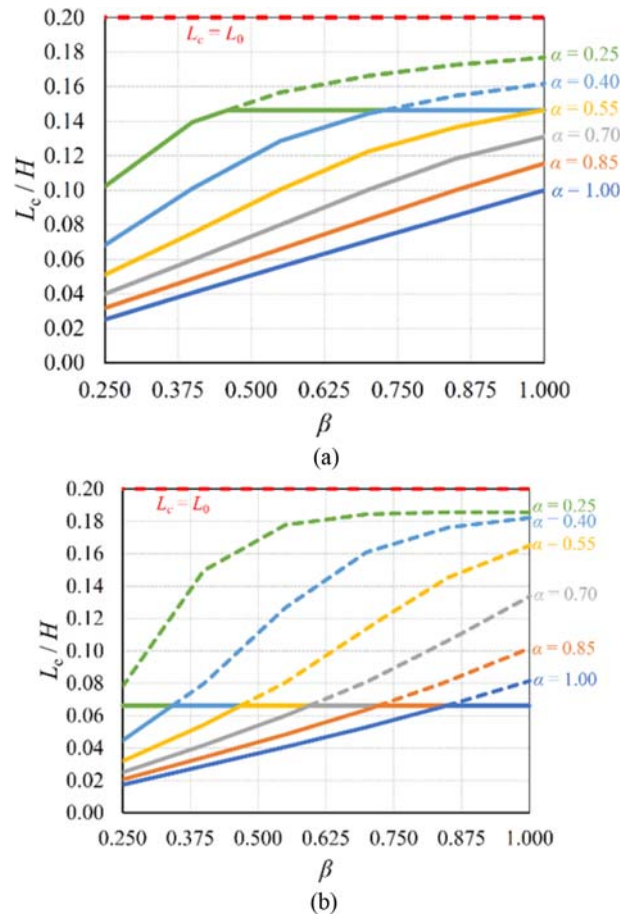


Fig. 21. Sensitivity of  $L_c$  with respect to Parameters  $\alpha$  and  $\beta$ : (a) Strong y-Direction, (b) Weak z-Direction

		sectional SD ( $\alpha$ )					
		0.25	0.40	0.55	0.70	0.85	1.00
sectional DD ( $\beta$ )	1.00	0.14	0.14	0.14	0.11	0.11	0.10
	0.85	0.14	0.14	0.13	0.10	0.10	0.08
	0.70	0.14	0.14	0.12	0.08	0.08	0.07
	0.55	0.14	0.13	0.10	0.06	0.06	0.05
	0.40	0.14	0.10	0.07	0.05	0.05	0.04
	0.25	0.10	0.07	0.05	0.03	0.03	0.02

(a)

		sectional SD ( $\alpha$ )					
		0.25	0.40	0.55	0.70	0.85	1.00
sectional DD ( $\beta$ )	1.00	0.06	0.06	0.06	0.07	0.07	0.07
	0.85	0.06	0.06	0.07	0.06	0.06	0.07
	0.70	0.07	0.07	0.07	0.06	0.06	0.05
	0.55	0.07	0.07	0.07	0.05	0.05	0.04
	0.40	0.07	0.07	0.05	0.03	0.03	0.03
	0.25	0.07	0.04	0.03	0.02	0.02	0.02

(b)

Fig. 22. Values of Actual  $L_c/H$  with respect to Parameters  $\alpha$  and  $\beta$ : (a) Strong y-Direction, (b) Weak z-Direction

procedure is free from numerical localization and can be used as a control tool for such more sophisticated analyses. However, some limits must be considered, and extension to more general conditions is currently under development: the procedure is only applicable to sufficiently slender cantilever piers for which shear deformations can be neglected; it neglects the behavior of the pier after peak strength of the cross-section, and applies only to the computation of the monotonic pushover curves; finally, the effects of deck stiffness is ignored.

Curvature profiles are obtained and can be used to accurately evaluate the equivalent plastic hinge length  $L_c$  for beam finite element analyses.

The case study of a rectangular hollow RC pier was considered to perform a parametric study on the influence of non-uniform deterioration, modeled by a two-parameter family of bilinear sectional responses.

The analyses showed that residual pier strength RPS and ductility RPD can be significantly influenced by the sectional degradation  $\alpha$  and  $\beta$  with global effects often stronger than the sectional ones. Indeed, the RPS is exactly equal to that of the resisting bending capacity of the base cross-section, governed by parameter  $\alpha$ , while it is not influenced by cross-section ductility variation, governed by parameter  $\beta$ . By contrast, the RPD depends on both parameters. Reduction of cross-section ductility ( $\beta$ ) directly traduces in a decrease of RPD, which can reduce up to 0.7 times the value of  $\beta$ . Reduction of cross-section bending strength ( $\alpha$ ) usually produces also a reduction of cross-section stiffness (Priestley et al., 2007), and thus leads to an increase of RPD, which can grow up to 10 times the value of  $\alpha$ .

It was also observed that the utilizable displacement capacity of the pier does not depend on the cross-section ductility variation  $\beta$ , as opposed to the actual one.


As concern the equivalent plastic hinge length, the analyses showed that, depending on the strength degradation, deteriorated and plain parts of the pier can exhibit significantly different deformation levels that affect the evolution of  $L_c$ , although its value is limited to an upper bound related to the extension  $L_0$  of the deteriorated part of the pier. Indeed, when cross-section strength ( $\alpha$ ) decreases, inelastic bending curvatures were observed to localize over  $L_0$ . This effect is more pronounced in more slender piers that reach higher deformation levels.

## Acknowledgments

P. Di Re acknowledges the research grant SEED PNR 2021 - 000048 21 SEED DI RE - CUP B89J21032850001 (Sapienza University of Rome).

## ORCID

Paolo Di Re  <https://orcid.org/0000-0002-3093-2728>

Davide Bernardini  <https://orcid.org/0000-0002-3683-9831>

Daniela Ruta  <https://orcid.org/0000-0002-2478-8934>

Achille Paolone  <https://orcid.org/0000-0002-1954-4724>

## References

- Babazadeh A, Burgueno R, Silva P (2016) P- $\delta$  effects on the plastic region of RC bridge columns: Closed-form solution. *Journal of Structural Engineering - ASCE* 142(11):04016116, DOI: 10.1061/(ASCE)ST.1943-541X.0001595
- Bae S, Bayrak O (2008) Plastic hinge length of reinforced concrete columns. *ACI Structural Journal* 105(3):290-300, DOI: 10.14359/19788
- Bairan JM, Mari AR (2007) Multiaxial-coupled analysis of RC cross-sections subjected to combined forces. *Engineering Structures* 29:1722-1738, DOI: 10.1016/j.engstruct.2006.09.007
- Barros H, Silva V, Ferreira C (2010) Second order effects in slender concrete columns - Reformulation of the Eurocode 2 method based on nominal curvature. *Engineering Structures* 32(12):3989-3993, DOI: 10.1016/j.engstruct.2010.08.005
- Bernardini D, Braga F, Buttarazzi F, Cardone D, Di Re P, Migliorino P, Paolone A, Rossi A, Ruta D (2023) Influence of spatially heterogeneous deterioration patterns on strength and ductility of corroded reinforced concrete bridge piers. *XIX ANIDIS Conference, Seismic Engineering in Italy Procedia Structural Integrity* 44:649-656, DOI: 10.1016/j.prostr.2023.01.085
- Bernardini D, Carbone G, Di Re P, La Morgia M, Mei A, Paolone A, Ruta D (2022) OpenSeesPy-based web application for pushover curve computation of RC bridge piers subject to arbitrarily non-uniform corrosion patterns. 2022 Eurasian OpenSees Days. *Lecture Notes in Civil Engineering*, 86-96, DOI: 10.1007/978-3-031-30125-4\_8
- Bernardini D, Ruta D, Di Re P, Paolone A (2021) Modeling non-uniform corrosion in reinforced concrete bridge piers. *Lecture Notes in Civil Engineering* 200:372-379, DOI: 10.1007/978-3-030-91877-4\_43
- Billah A, Alam M (2016) Plastic hinge length of shape memory alloy (SMA) reinforced concrete bridge pier. *Engineering Structures* 117:321-331, DOI: 10.1016/j.engstruct.2016.02.050
- Bimschas M (2010) Displacement based seismic assessment of existing bridges in regions of moderate seismicity
- Burgueno R, Babazadeh A, Fedak LK, Silva PF (2016) Second-order effects on seismic response of slender bridge columns. *ACI Structural Journal* 113(4):735-746, DOI: 10.14359/51688751
- Cassese P, De Risi M, Verderame G (2019) A modelling approach for existing shear-critical RC bridge piers with hollow rectangular cross section under lateral loads. *Bulletin of Earthquake Engineering* 17:237-270, DOI: 10.1007/s10518-018-0429-2
- Cassese P, Ricci P, Verderame G (2017) Experimental study on the seismic performance of existing reinforced concrete bridge piers with hollow rectangular section. *Engineering Structures* 144:88-106, DOI: 10.1016/j.engstruct.2017.04.047
- Castaldo P, Gino D, Marano GC, Mancini G (2022) Aleatory uncertainties with global resistance safety factors for non-linear analyses of slender reinforced concrete columns. *Engineering Structures* 25:113920, DOI: 10.1016/j.engstruct.2022.113920
- Ceresia P, Petrini L, Pinho R (2007) Flexure-shear fiber beam-column elements for modeling frame structures under seismic loading - State of the art. *Journal of Earthquake Engineering* 11:46-88, DOI: 10.1080/13632460701280237
- Chen X, Xia X, Zhang X, Gao J (2020) Seismic performance and design of bridge piers with rocking isolation. *Structural Engineering and Mechanics* 73(4):447-454, DOI: 10.12989/sem.2020.73.4.447
- Delgado R, Delgado P, Vila Pouca N, Arède A, Rocha P, Costa A (2009)

- Shear effects on hollow section piers under seismic actions: Experimental and numerical analysis. *Bulletin of Earthquake Engineering* 7(2): 377-389, DOI: [10.1007/s10518-008-9098-x](https://doi.org/10.1007/s10518-008-9098-x)
- Di Re P, Addressi D (2022) Computational enhancement of a mixed 3D beam finite element with warping and damage. *Journal of Applied and Computational Mechanics* 8(1):260-281, DOI: [10.22055/JACM.2021.37948.3120](https://doi.org/10.22055/JACM.2021.37948.3120)
- Di Re P, Addressi D, Filippou FC (2018) Mixed 3D beam element with damage plasticity for the analysis of RC members under warping torsion. *Journal of Structural Engineering - ASCE* 144(6):04018064, DOI: [10.1061/\(ASCE\)ST.1943-541X.0002039](https://doi.org/10.1061/(ASCE)ST.1943-541X.0002039)
- Di Re P, Bernardini D, Ruta D, Paolone A (2022) A simple numerical approach for the pushover analysis of slender cantilever bridge piers taking into account geometric nonlinearity. *Asian Journal of Civil Engineering* 23:455-469, DOI: [10.1007/s42107-022-00433-z](https://doi.org/10.1007/s42107-022-00433-z)
- Domaneschi M, De Gaetano A, Casas JR, Cimellaro GP (2020) Deteriorated seismic capacity assessment of reinforced concrete bridge piers in corrosive environment. *Structural Concrete* 21:1823-1838, DOI: [10.1002/suco.202000106](https://doi.org/10.1002/suco.202000106)
- European Committee for Standardization (2005) Eurocode 8: Design of structures for earthquake resistance. Part 1, EN 1998-1
- Fenwick R, Davidson B, Chung B (1992) P-delta actions in seismic resistant structures. *Bulletin of the New Zealand Society for Earthquake Engineering* 25(1):56-69, DOI: [10.5459/bnzsee.25.1.56-69](https://doi.org/10.5459/bnzsee.25.1.56-69)
- Gaiotti R, Smith B (1989) P-Delta analysis of building structures. *Journal of Structural Engineering - ASCE* 115(4):755-770, DOI: [10.1061/\(ASCE\)0733-9445\(1989\)115:4\(755\)](https://doi.org/10.1061/(ASCE)0733-9445(1989)115:4(755))
- Kashani M, Maddocks J, Dizaj E (2019) Residual capacity of corroded reinforced concrete bridge components: State-of-the-art review. *Journal of Bridge Engineering* 24(7):1-16, DOI: [10.1061/\(ASCE\)BE.1943-5592.0001429](https://doi.org/10.1061/(ASCE)BE.1943-5592.0001429)
- Li D, Wei R, Xing F, Sui L, Zhou Y, Wang W (2018) Influence of Non-uniform corrosion of steel bars on the seismic behavior of reinforced concrete columns. *Construction and Building Materials* 167:20-32, DOI: [10.1016/j.conbuildmat.2018.01.149](https://doi.org/10.1016/j.conbuildmat.2018.01.149)
- Lignola GP, Fabbrocino F, Prota A, Cosenza E, Manfredi G (2023) Reinforcement corrosion in RC hollow piers: Destructive and non-destructive tests. *Materials* 16(7):2790, DOI: [10.3390/ma16072790](https://doi.org/10.3390/ma16072790)
- Mahboubi S, Kioumarsis M (2021) Damage assessment of RC bridges considering joint impact of corrosion and seismic loads: A systematic literature review. *Construction and Building Materials* 295:123662, DOI: [10.1016/j.conbuildmat.2021.123662](https://doi.org/10.1016/j.conbuildmat.2021.123662)
- Mander J, Priestley M, Park R (1988) Theoretical stress-strain model for confined concrete. *Journal of Structural Engineering - ASCE* 114(8): 1804-1826, DOI: [10.1061/\(ASCE\)0733-9445\(1988\)114:8\(1804\)](https://doi.org/10.1061/(ASCE)0733-9445(1988)114:8(1804))
- Meda A, Mostosi S, Rinaldi Z, Riva P (2014) Experimental evaluation of the corrosion influence on the cyclic behaviour of RC columns. *Engineering Structures* 76:112-123, DOI: [10.1016/j.engstruct.2014.06.043](https://doi.org/10.1016/j.engstruct.2014.06.043)
- OpenSees (2021) The openseespy library, <https://openseespydoc.readthedocs.io/en/latest/index.html>
- Park R, Paulay T (1975) Reinforced concrete structures. Wiley-Interscience publication, John Wiley & Sons
- Pokhrel M, Bandelt M (2019) Plastic hinge behavior and rotation capacity in reinforced ductile concrete flexural members. *Engineering Structures* 200(2019):109699, DOI: [10.1016/j.engstruct.2019.109699](https://doi.org/10.1016/j.engstruct.2019.109699)
- Pozo JD, Hube MA, Kurama YC (2022) Effective nonlinear simulations of RC columns with force-based elements. *Journal of Earthquake Engineering* 1-22, DOI: [10.1080/13632469.2021.2001395](https://doi.org/10.1080/13632469.2021.2001395)
- Priestley M, Calvi G, Kowalsky M (2007) Displacement based seismic design of structures. Iuss Press
- Rinaldi Z, Di Carlo F, Spagnuolo S, Meda A (2022) Influence of localised corrosion on the cyclic response of reinforced concrete columns. *Engineering Structures* 256:114037, DOI: [10.1016/j.engstruct.2022.114037](https://doi.org/10.1016/j.engstruct.2022.114037)
- Rinaldi Z, Valente C, Pardi L (2008) A simplified methodology for the evaluation of the residual life of corroded elements. *Structure and Infrastructure Engineering* 4(2):139-152, DOI: [10.1080/15732470601155540](https://doi.org/10.1080/15732470601155540)
- Saritas A, Filippou FC (2009) Inelastic axial-flexure-shear coupling in a mixed formulation beam finite element. *International Journal of Non-Linear Mechanics* 44:913-922, DOI: [10.1016/j.ijnonlinmec.2009.06.007](https://doi.org/10.1016/j.ijnonlinmec.2009.06.007)
- Scott M, Fenves G (2006) Plastic hinge integration methods for force-based beam-column elements. *Journal of Structural Engineering - ASCE* 132(2):244-252, DOI: [10.1061/\(ASCE\)0733-9445\(2006\)132:2\(244\)](https://doi.org/10.1061/(ASCE)0733-9445(2006)132:2(244))